Supporting Information

-

Size Effects in the Oscillatory Rotation Dynamics of Ni Nanorods in Poly(ethylene oxide) Solutions

Micha Gratz and Andreas Tschöpe *

Experimentalphysik, Campus D2 2, Universität des Saarlandes, 66123 Saarbrücken, Germany

**E-mail: a.tschoepe@nano.uni-saarland.de*

Contents

S1 Macroscopic properties of PEO solutions

S1.1 Intrinsic viscosity and Flory exponent

The PEO macromolecules for micro- and macrorheological investigations were purchased from *Polymer Standards Service GmbH, Mainz, Germany*. Certificates of the molar mass distribution (GPC/SEC) and derived weight averages were provided by the supplier. The characteristic properties of weight average molar mass M_w, number average molar mass M_n, molar mass at peak maximum M_p, polydispersity index $PDI = M_w/M_n$ and the order number are summarized in Table S1.

Table S1: Characteristic properties of PEO polymers: polymer ID, weight average molar mass M_w, number average molar mass M_n, molar mass at peak maximum M_p, polydispersity index $PDI = M_w/M_n$ and the order number.

ID	M_w [kg/mol]	M_n [kg/mol]	M_p [kg/mol]	$PDI = M_w/M_n$	Order No.
PEO-50k	53	49.5	54	1.07	PSS-peo50k
PEO-110k	106	101	106	1.05	PSS-peo110k
PEO-220k	220	197	222	1.11	PSS-peo220k
PEO-500k	480	398	450	1.21	PSS-peo500k
PEO-1M	1020	884	969	1.15	PSS-peo1m

The viscosity at $T = 23.00 \pm 0.02\,^{\circ}\mathrm{C}$ of the solvent (water) and dilute polymer solutions were determined using a rolling ball viscometer. The relative viscosities $\eta_r = \eta/\eta_s$ and the specific viscosities $\eta_{sp} = (\eta - \eta_s)/\eta_s$ were calculated and analyzed according to the Huggins equation [1],

$$\frac{\eta_{sp}}{c} = [\eta] + k_H[\eta]^2 c\,, \tag{S1}$$

and the Kraemer equation [2],

$$\frac{\ln(\eta_r)}{c} = [\eta] + \left(k_H - \frac{1}{2}\right)[\eta]^2 c\,. \tag{S2}$$

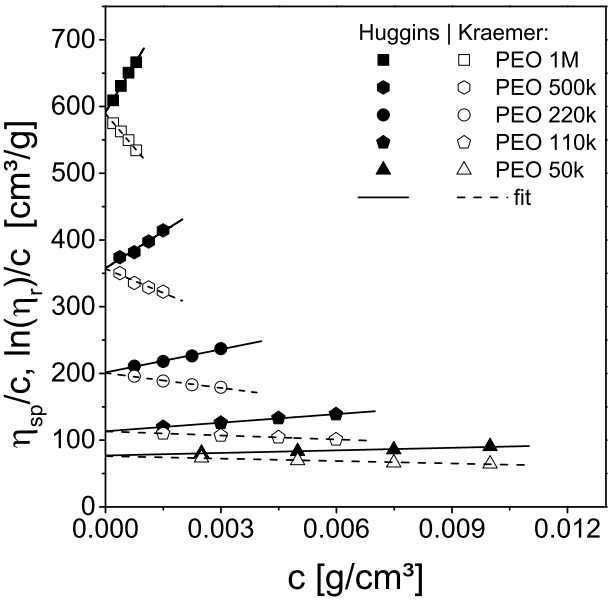

Figure S1: Calculated values of η_{sp}/c and $\ln(\eta_r)/c$ from rolling ball viscometer measurements of dilute PEO solutions (symbols) with fits, using Equation S1 (line) and S2 (dashed line), to determine the mean intrinsic viscosities $[\eta]$ based on both method.

Table S2: Fitting results of intrinsic viscosity $[\eta]$ and Huggins constant k_H using Huggins equation S1 and Kraemer equation S2.

ID	Huggins		Kraemer	
	$[\eta]$ [cm^3/g]	k_H	$[\eta]$ [cm^3/g]	k_H
PEO-50k	77(1)	0.22(3)	76(1)	0.29(2)
PEO-110k	113(1)	0.33(1)	113(1)	0.34(1)
PEO-220k	202(2)	0.35(2)	201(1)	0.31(1)
PEO-500k	358(4)	0.29(4)	357(3)	0.31(2)
PEO-1M	591(3)	0.27(2)	589(1)	0.30(1)

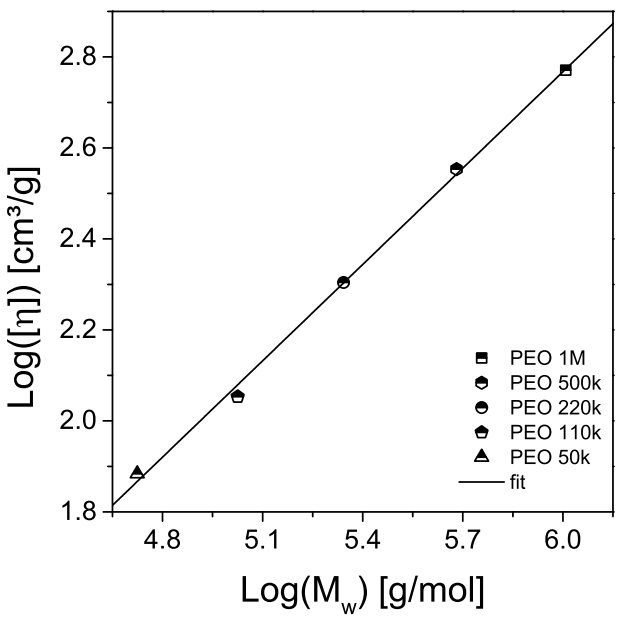

Figure S2: Log-Log-plot of the mean intrinsic viscosity $[\eta]$ (Table S2) as function of molecular mass M_w with linear fit to derive the parameters $\alpha = 0.71(2)$ and $K = 0.032(7)\,(\mathrm{cm}^3/\mathrm{g})(\mathrm{mol}/\mathrm{g})^{0.71(2)}$ in the Mark-Houwink equation, $[\eta] = K\,M_w^{\alpha}$. Based on the parameter α we calculated the Flory exponent $\nu = (\alpha+1)/3 = 0.570(7)$.

S1.2 Intrinsic length scales

The primary intrinsic length scale is the size of the macromolecules in solution. The radius of gyration is often used mainly for practical reasons as it can be determined by scattering experiments. We use the empirical relationship, $R_g^{LS} = 0.202\, M_w^{0.58}$ Å, derived from light scattering by Kawaguchi et al. [3]. Another characteristic measure for the size of the polymer chain is the root-mean-square end-to-end distance $R_{ee} = \langle R^2 \rangle^{1/2} = bN^\nu$, where b is the size of a Kuhn monomer and $N = M_w/M_0$ the number of monomers, with molar mass M_0, per chain. Because of inconsistent results when using values, tabulated for the melt, we used as Kuhn monomer size in solution $b = 8.7$ Å and corresponding $M_0 = 108$ g/mol $\sim b$, which were obtained by fitting the radius of gyration [4] $R_g = bN^\nu/((2\nu+1)(2\nu+2))^{1/2}$ to the empirical relationship, $R_g^{LS} = 0.202\, M_w^{0.58}$ Å [3]. The same segment length b was also derived in the latter reference.

In dilute solutions, the radius of gyration R_{g0} of the molecules and the correlation length $\xi_0 = R_{g0}/\sqrt{3}$, e.g. determined from the light scattering structure factor, are independent of concentration c. At the overlap volume fraction ϕ^*, the polymer coils are space filling and R_g as well as ξ are concentration dependent [5] for $\phi > \phi^*$. The radius of gyration decreases weakly as $R_g(\phi) \approx R_{g0}(\phi/\phi^*)^{-(2\nu-1)/(6\nu-2)} \sim (\phi/\phi^*)^{-0.1}$ due to the screening of excluded volume interaction and approaches the ideal chain value $R_{g,m} = bN^{1/2}/\sqrt{6}$ in the melt. In the semi-dilute regime, the correlation length decreases due to coil interpenetration, $\xi \approx \xi_0(\phi/\phi^*)^{-\nu/(3\nu-1)} \sim (\phi/\phi^*)^{-0.8}$ and is independent of the polymer molar mass. The volume fraction Φ^{**}, at which $\xi = b$ marks the upper limit of the semi-dilute and the transition to the concentrated solution regime [4].

Solutions of large macromolecules above the entanglement concentration c_e exhibit a strong increase in viscosity $\sim M_w^{3.4}$, transient network elasticity with a plateau modulus G^0, and crossover, $G'(\omega_c) = G''(\omega_c)$. The mechanism behind these features were disclosed in the reptation theory by de Gennes [6] and Doi and Edwards [7]. Entanglements with other chains confine the lateral motion of a macromolecule into an effective tube such that stress relaxation relies on the evacuation of this tube by curvilinear diffusion. With two major corrections of the theory to account for contour length fluctuations (CLF) and constraint release (CR), the characteristic tube size a_t and relaxation time constants can be obtained by quantitative analysis of experimental data [8]. Contour length fluctuations are the result of higher than zero-order Rouse modes and can be incorporated into the classical reptation model by introducing a renormalized plateau modulus and reptation time, represented by a polynomal function of the number of entanglements per chain, $Z = M/M_e$, with molar mass M_e of the chain segment between entanglements (entanglement strand) [9]. Constraint release (tube renewal) takes the dynamic nature of entanglements caused by moving chains into account [10]. In the Likhtman-McLeish (L-ML) model, the coefficients of the CLF correction were obtained by fitting simulated stress relaxation functions for given values of Z. Furthermore, an additional parameter c_v was introduced to adjust the jump distance of a chain segment after constraint release in relation to

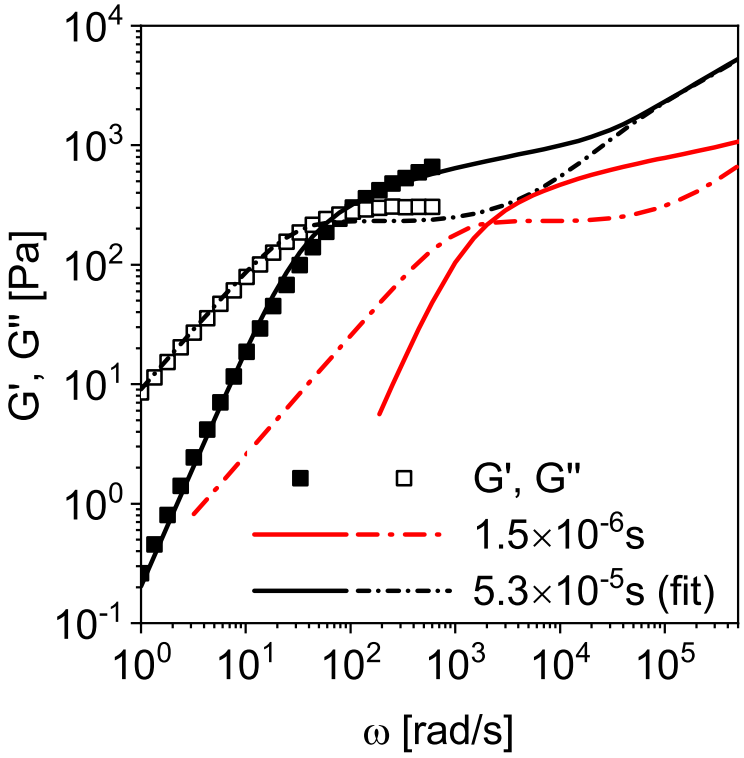

Figure S3: Dynamic modulus of 5.29 wt.% PEO-1M solution measured by small amplitude oscillatory shear with constant shear strain amplitude of 10 % over the angular frequency range $\omega = 1-600\ rad/s$. The modulus, predicted by the Likhtman-McLeish model with all parameters fixed at $G_e = 1306\,\mathrm{Pa}$, $M_e = 116500\,\mathrm{g/mol}$, $c_v = 0.1$ and $\tau_e = 1.5\times10^{-6}\,\mathrm{s}$ (red) is shifted to high frequencies. A fit with τ_e as variable parameter (black lines) resulted in a good agreement in the accessible frequency range.

the tube diameter a_t. This model has been incorporated in the analysis tool box of the open-source package RepTate, provided by J. Ramirez and V. Boudara [11]. Model parameters are the entanglement modulus G_e (please notice the difference to G^0 as discussed in [8]), the molar mass M_e and Rouse equilibration time constant τ_e of an entanglement strand, and the CR parameter c_v. For given polymer molar mass M and temperature T, these parameters could be retrieved by fitting G' and G'' spectra and further characteristic quantities such as Z, a_t, the disengagement τ_D and the Rouse time of the whole chain derived. In principle, the same approach could be applied to semi-dilute polymer solutions if the incomplete screening of excluded volume- and hydrodynamic interactions is taken into account.

The macroscopic dynamic modulus of 5.29 wt% PEO-1M-solution is shown in Figure S3. The storage and loss modulus exhibit the expected power law relations, $G' \sim \omega^2$ and $G'' \sim \omega$ in the terminal region and a crossing point at $\omega_c = 91\,\mathrm{rad/s}$ which translates into a characteristic time constant $\tau_c = 1/\omega_c = 11 \times 10^{-3}\,\mathrm{s}$. However, the SAOS data represent only a minor fraction of the entire dynamic modulus spectrum, which is insufficient for reasonable model fitting. In contrast to polymer melts, the

number Z of entanglements per chain can be small and their contribution to the dynamic modulus rather weak even at large molar mass. For lack of this approach to determine the characteristic parameters directly from experiment, we used tabulated values for the PEO melt ($a(1) = 37\,\text{Å}$, entanglement strand molar mass $M_e(1) = 1700\,\text{g/mol}$, and entanglement modulus $G_e(1) = 1.8 \times 10^6\,\text{Pa}$) and the appropriate scaling relations for extrapolation to semi-dilute solutions [5]. Model calculation based on these parameter are compared with experimental results as a test for plausibility.

For the particular 5.29 wt% PEO-1M solution, the entanglement modulus is $G_e \approx G_e(1)\phi^{3\nu/(3\nu-1)} \approx 1306\,\text{Pa}$ and the molar mass per entanglement strand $M_e \approx M_e(1)\phi^{-1/(3\nu-1)} \approx 116500\,\text{g/mol}$. In contrast to these two parameters, computation of the characteristic time constants is more involved. The disengagement time in the uncorrected Doi-Edwards model $\tau_d = 3Z^3\tau_e$, where τ_e is the Rouse rotational relaxation time of an entanglement strand [7, 12]. In semi-dilute solution, however, hydrodynamic and excluded volume interactions are effective below their characteristic screening length, which is of the same order of magnitude as the correlation length ξ [5]. The macromolecule chain is a random walk of correlation blobs [5, 13] with size ξ, each containing $g \approx \rho_m\xi^3$ monomers, where $\rho_m = (cNN_A)/M_w$ is the monomer density [4]. Due to hydrodynamic interaction, relaxation within the correlation blobs is fast and determined by their Zimm time $\tau_\xi = (2\sqrt{3\pi})^{-1}(\eta_s/(k_BT))\xi^3$. The rotational relaxation time of the entire molecule $\tau_{ch} = (3\pi^2)^{-1}\tau_\xi(N/g)^2$ is twice the Rouse time for a chain of N/g effective segments, each with relaxation time τ_ξ. The equilibration time of an entanglement strand is $\tau_e = \tau_{ch}/Z^2$. For the 5.29 wt% PEO-1M solution, this calculation results in $\tau_e \approx 1.5 \times 10^{-6}\,\text{s}$. The last model parameter, c_v, cannot be evaluated independently so we used values between $c_v = 0$ as the lower and $c_v = 1$, i.e. jump distance a_t, as physically plausible upper limit.

The result of the Likhtman-McLeish model calculation for the given parameters, shown in Figure S3 (red color), apparently reflects the overall shape of the dynamic modulus in the measured range, but the plateau region is located at too high frequencies. Please notice that any variation in τ_e merely shifts the modulus along frequency axis whereas the shape remains unaltered. Keeping the values for all model parameters fixed except for the equilibration time constant, a fitting procedure provided $\tau_e = 3.2 \times 10^{-5}\,\text{s}$ ($c_v = 0$) and $\tau_e = 9.8 \times 10^{-5}\,\text{s}$ ($c_v = 1$). The static parameters G_e and M_e of the entanglements network, that were extrapolated from the tabulated values of the PEO melt, provided a good agreement with the experimental data in the measured frequency range. Hence, the extrapolated tube diameter a_t is also a reasonable estimate for the semi-dilute PEO solutions. The limited descriptive power with respect to absolute time constants is not surprising since the treatment of hydrodynamic screening in the blob model is approximate only and not intended for quantitative modelling.

S2 Ni nanorods

S2.1 TEM images of the nanorods N2 - N5

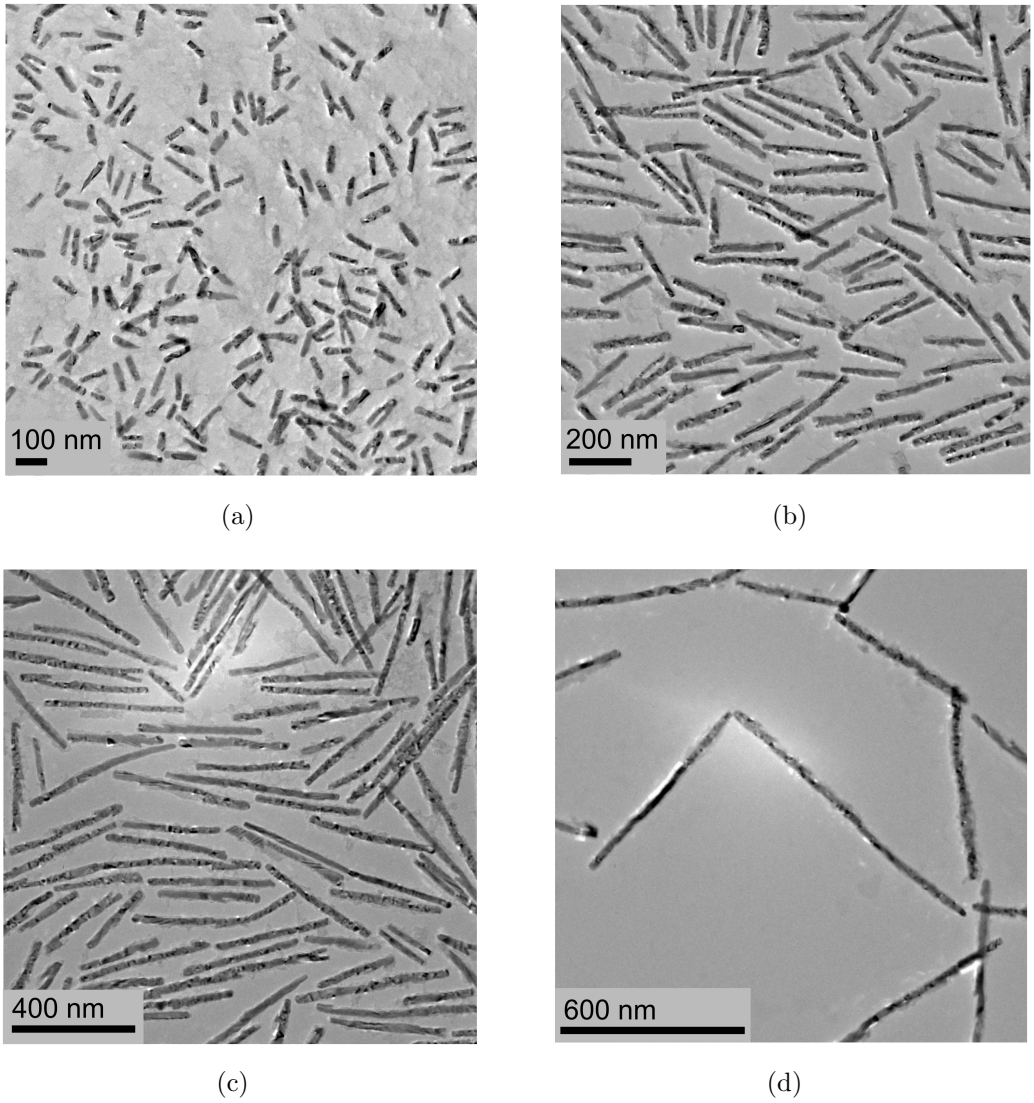

Figure S4: TEM images of the nanorod samples (a) N2 (b) N3 (b) N4 and (c) N5. The result for sample N1 is shown in the main text.

S2.2 Static field-dependent optical transmission (SFOT) measurements

This methods takes advantage of the collinear uniaxial ferromagnetic and optical anisotropy, with different optical extinction cross sections $\langle C_{ext,L} \rangle$ and $\langle C_{ext,T_{1,2}} \rangle$ for longitudinal and the two transversal polarization directions relative to the rod

axis. The optical transmittance along a path s through a dilute dispersion of N_r nanorods per unit volume in a transparent matrix follows the Beer-Lambert law, $I/I_0 = \exp(-sN_r\langle C_{ext}\rangle)$, with the incident and transmitted intensities I_0 and I, respectively. In zero field, i.e. at isotropic orientation distribution, the mean extinction cross section $\langle C_{ext}\rangle_x = (C_{ext,L} + C_{ext,T_1} + C_{ext,T_2})/3$. With increasing external field H, alignment of the nanorods against thermal energy results in a characteristic field-dependent transmittance. In the transmittance of linearly polarized light, normalized to the zero-field transmittance,

$$I(H)_{\perp,\parallel}/I_\times = \exp\left(-Ns(\langle C_{\text{ext}}\rangle_{\perp,\parallel}(H) - \langle C_{\text{ext}}\rangle_\times)\right), \tag{S3}$$

the field-dependent mean optical cross sections $\langle C_{\text{ext}}\rangle_{\perp,\parallel}(H)$ are different for field direction perpendicular and parallel to the optical polarization direction, respectively. The ensemble average is determined by the second moment $\langle\cos^2\beta\rangle$ of the distribution function of the angle β between the magnetic moment (rod axis) and the field direction, and is given by

$$\langle\cos^2\beta\rangle = 1 + 2/\zeta^2 - 2\coth(\zeta)/\zeta. \tag{S4}$$

The mean magnetic moment is obtained by fitting the Langevin parameter ζ. Further details can be found in Ref. [14].

As shown in Figure S5 for the nanorod sample N1 in water, the transmitted intensity $I_\perp$, normalized to the zero field intensity I_x, increased with magnetic field and decreased for $I_\parallel$, as expected for the lower electrical polarizability of the nanorods along the short as compared to the long rod axis. The measurements were analyzed as described in Reference [14] to obtain the mean magnetic moment per particle m and the particle density N in the colloid.

With increasing magnetic field, the transmission saturates until all nanorods in the colloid are aligned along the field. At a sufficiently large value of the Langevin parameter, e.g. $\zeta > 30$, the transmitted intensity depends on the orientation angle of the rod axis with respect to polarization direction and vice versa, $\vartheta = \sin^{-1}((I - I_{||})/(I_\perp - I_{||}))^{1/2}$, Figure S5. SFOT data for all nanorods used in the microrheological measurements are presented in Figure S6.

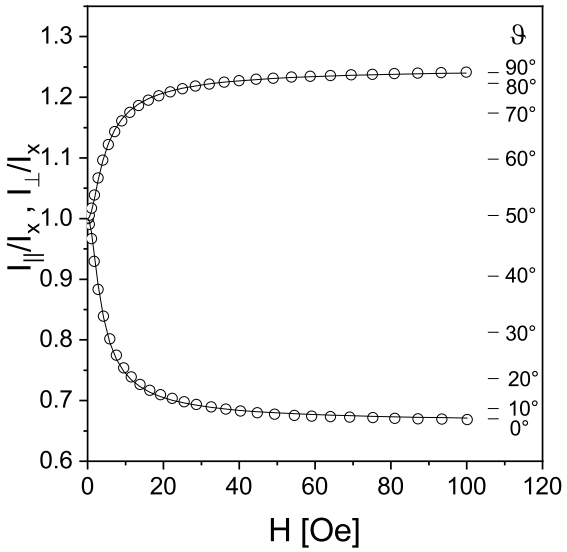

Figure S5: SFOT measurement of sample N1 with normalized optical transmission $I_\perp/I_x$ (upper branch) and $I_\parallel/I_x$ (lower branch) as function of field H. The regression analysis (lines) (see Ref. [14]) provided the mean magnetic moment $m = 3.84(1) \times 10^{-17}\,\mathrm{Am}^2$. The intensity of the sample with nanorods aligned under saturation field depends on the angle ϑ between the rod axis and the polarization direction.

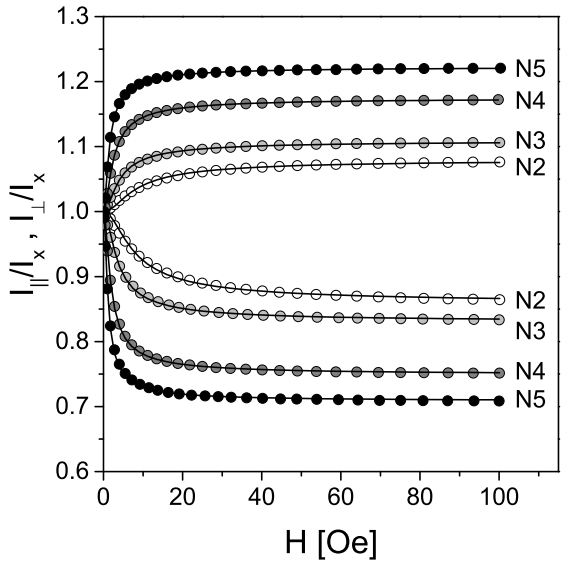

Figure S6: SFOT measurements of sample N2-5 with normalized optical transmissions $I_\perp/I_x$ (upper branches) and $I_\parallel/I_x$ (lower branches). Because the magnetic moment m increases with the length of the nanorods, magnetic saturation was reached at lower fields H for the larger nanorods. The splitting of the two branches depends on the aspect ratio of the nanorods and their concentration in the colloid. Solid lines represent fit results (lines) based on eq. S3 and model calculations as described in Ref. [14].

S3 Oscillating field-dependent optical transmission (OFOT) measurements

S3.1 Dynamic modulus G^* and optical response function X^*

We assume the polymer solution to be isotropic, homogeneous, incompressible and to exhibit linear viscoelastic behavior at the applied strain. The general expression for the time-dependent simple shear stress τ and strain γ is a linear differential equation with constant coefficients a_n and b_m [15],

$$\sum_n a_n \tau^{(n)} = \sum_m b_m \gamma^{(m)}, \tag{S5}$$

where $(\cdot)^{(i)}$ denotes the time derivative $d^i(\cdot)/dt^i$. Inserting complex harmonic functions $\tau^*(t) = \tau_0^* \exp \mathrm{i}\omega t$ and $\gamma^*(t) = \gamma_0^* \exp \mathrm{i}\omega t$ leads to

$$\tau_0^* \sum_n a_n (\mathrm{i}\omega)^n = \gamma_0^* \sum_m b_m (\mathrm{i}\omega)^m. \tag{S6}$$

The dynamic modulus,

$$G^*(\omega) = \frac{\tau_0^*}{\gamma_0^*} = \frac{\sum_m b_m (\mathrm{i}\omega)^m}{\sum_n a_n (\mathrm{i}\omega)^n}, \tag{S7}$$

is completely determined by the coefficients a_n and b_m.

The instrumental quantities measured in macrorheology, e.g. the mechanical torque applied onto the shaft of a cone-plate system and the shaft rotation angle, are translated into geometry-independent variables, i.e. shear strain and stress. In active microrheology, the force and torque applied to the probe particles and the geometry-dependent deformation of the matrix have to be included explicitly in the model. The mechanical interaction between the rotating nanoparticle and the suspension medium includes viscous torque $T_v = K_v \eta \dot{\theta}$ and elastic restoring torque $T_e = K_v G \theta$ [1]. The geometry factor K_v is determined by the shape and hydrodynamic size of the inclusion and is related to the rotational diffusion constant $D_r = \xi_r / k_B T = K_v \eta / k_B T$.

[1] At the viscosity of pure water, the contribution of inertial torque at the maximum frequency (f=3 kHz) is approximately 10% of the frictional torque. Such low viscosities are considered as lower resolution limit. For all measurements of zero-shear rate viscosity (low frequency) in semi-dilute solutions and of the dynamic modulus in the entanglement regime, inertial effects can be neglected.

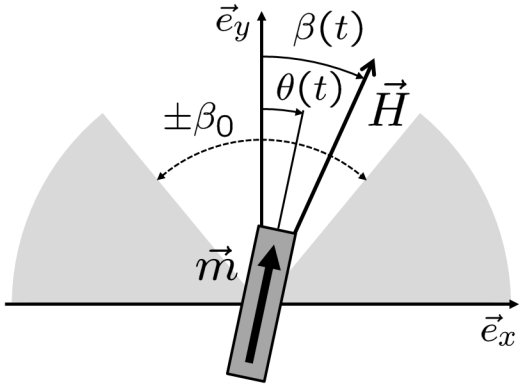

Figure S7: Schematic diagram to illustrate the oscillating motion of an unaxial magnetic particle with magnetic moment m exposed to a magnetic field of constant magnitude H_0 and direction $\beta(t)$ oscillating within an angular range of $\pm\beta_0$. The OFOT response function is determined by the time-dependent orientation angles of the magnetic moment, $\theta(t) = \theta_0^* \sin(\omega t)$ with respect to the direction of the field, $\beta(t) = \beta_0 \sin(\omega t)$.

The relationship between the OFOT response function $X^*(\omega)$ and the complex dynamical modulus $G^*(\omega)$ can be derived for general linear viscoelastic matter. The equation of rotational motion for a torque-driven particle is given as

$$\sum_n a_n T^{(n)} = K_v \sum_m b_m \theta^{(m)} \tag{S8}$$

with the same coefficients a_n and b_m of the linear differential equation describing the properties of the viscoelastic matrix, eq S5. Substituting the torque, $T = m\mu_0 H_0 \sin(\beta - \theta) \approx m\mu_0 H_0(\beta - \theta)$, results in

$$\sum_n a_n (\beta - \theta)^{(n)} = K \sum_m b_m \theta^{(m)}, \tag{S9}$$

with $K = K_v / m\mu_0 H_0$. Inserting complex exponential harmonic functions (see above) and using the linearity of the differential equation,

$$\beta_0 \sum_n a_n (\mathrm{i}\omega)^n - \theta_0^* \sum_n a_n (\mathrm{i}\omega)^n = K\theta_0^* \sum_m b_m (\mathrm{i}\omega)^m. \tag{S10}$$

With the dynamic modulus, eq S7, we obtain $\beta_0 - \theta_0^* = K\theta_0^* G^*$ from which

$$X^*(\omega) = \frac{\theta_0^*}{\beta_0} = \frac{1}{1 + KG^*(\omega)} \tag{S11}$$

follows immediately.

This identity enables the computation of the complex modulus directly from the OFOT response function [16] provided the particle factor K is a single valued

constant. However, microrheological measurements based on ensembles of magnetic nanoparticles are severely affected by their polydispersity, which we take into account by introducing a distribution function $P(K)$, i.e.

$$X^*(\omega) = \int_0^\infty P(K)(1 + KG^*(\omega))^{-1} dK. \tag{S12}$$

The distribution function $P(K)$ represents the polydispersity of the nanorods regarding their hydrodynamic rotational friction factor ξ_r as well as their magnetic moment m. $P(K)$ is assumed to be characteristic for a given nanorod colloid. Hence, the distribution function can be calibrated by a reference measurement using a matrix phase with well defined dynamic modulus, e.g. $G^*(\omega) = \mathrm{i}\eta_0\omega$ for a Newtonian fluid with constant viscosity η_0. The task of retrieving $P(K)$ from the measured optical response function $X^*(\omega)$ is solved by numerical inversion with Tikononov regularization and Bayesian inference (see following section for details).

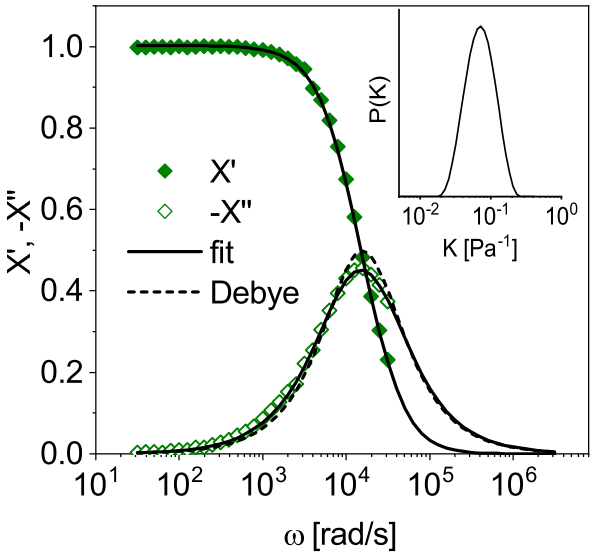

Figure S8: The OFOT spectrum of nanorods (N3) in water is slightly broadened as compared to a single Debye function (dashed) due to polydispersity. The distribution function $P(K)$ (insert) is retrieved by numerical inversion of the OFOT spectrum with the shown fit result.

The OFOT spectrum for Ni nanorods in water is shown in Figure S8. The relaxation peak in the imaginary part is slightly broadened as compared to a single Debye function indicating a moderate polydispersity of the nanorods. The distribution function $P(K)$ (insert) is retrieved by numerical inversion and is used in the following analysis of OFOT measurements of the same nanorod colloid in polymer solutions. Starting from an initial guess for the dynamic modulus, the optical response function is computed using eq. S12 with calibrated $P(K)$ followed by iterative refinement of G' and G'' until the best agreement with the measured data is obtained,

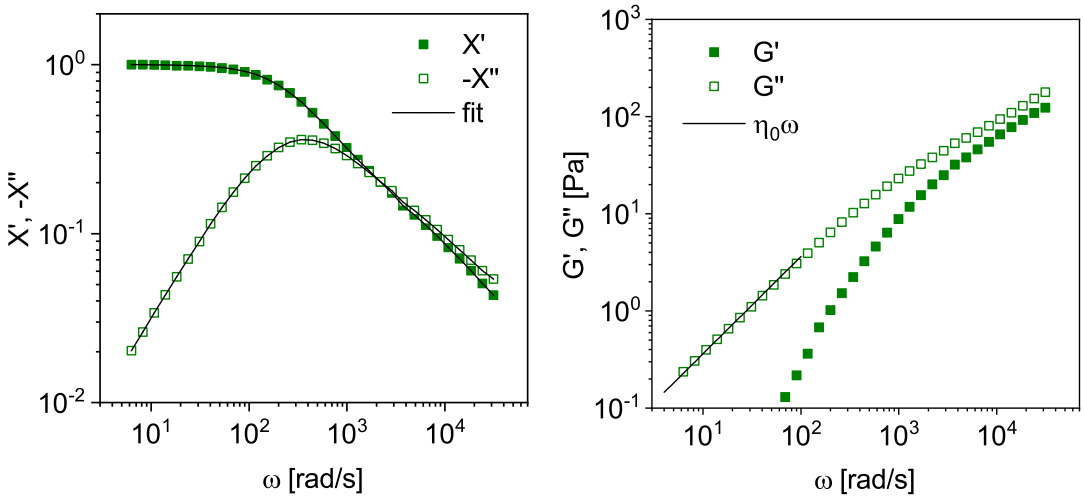

Figure S9: Example for the analysis of an OFOT-spectrum (log-log plot) of nanorods (N3) in 1.60 wt% PEO-1M (left). Fitting of experimental data using eq S12 and $P(K)$, obtained by numerical inversion of a calibration measurement, provided the corresponding dynamic modulus G' and G'' (right). The zero-shear rate viscosity η_0 is obtained from the prefactor in the linear regime.

Figure S9. The zero-shear rate viscosity is calculated from the loss modulus in the terminal region.

S3.2 Determination of $P(K)$ from a calibration measurement

The distribution function $P(K)$ represents the polydispersity of the nanorods regarding their hydrodynamic rotational friction factor ξ_r and their particle magnetic moment m. $P(K)$ is assumed to be characteristic for a given nanorod colloid and can be determined by a calibration measurement using a matrix phase with well defined dynamic modulus, e.g. $G^*(\omega) = \mathrm{i}\eta_0\omega$ for a Newtonian fluid with constant viscosity η_0. With Eq. S12,

$$X^*(\omega) = \int_0^\infty P(K)\frac{1}{1+\mathrm{i}K\eta_0\omega}dK. \tag{S13}$$

The task of retrieving $P(K)$ from the measured optical response function $X^*(\omega)$ is solved by numerical inversion with Tikononov regularization.. The measured optical response function is a vector with M complex valued data points. At each measured angular frequency ω_j, the value of X^* can be approximated by a weighted sum of model functions,

$$X^*(\omega_j) = \sum_{i=1}^{N} P(K_i)\frac{1}{1+\mathrm{i}K_i\eta_0\omega_j}\Delta K_i, \tag{S14}$$

where the distribution function $P(K)$ is also discretised into N bins of width ΔK_i being equally large on a logarithmic scale. Equation S14, can be written as $\mathrm{X}^* = \mathbf{A}^*\mathrm{p}$, where $A^*_{i,j} = (1+\mathrm{i}K_i\eta_0\omega_j)^{-1}$ are the elements of the transfer matrix and $p_i = P(K_i)\Delta K_i$ the elements of the coefficient vector to be determined. Assuming measurement uncertainties governed by gaussian noise with standard deviation σ, the best interpolant minimizes $\chi^2 = (1/\sigma^2)||\mathbf{A}^*\mathrm{p} - X^*||^2$. In order to suppress high frequency fluctuations, typically encountered with ill-conditioned inversion problems, exhaustive fitting of noise and also negative values of p_j, the coefficient vector p is obtained as the non-negative least square solution of the Tikhonov functional

$$T(\mathrm{p}) = \frac{1}{2\sigma^2}||\mathbf{A}^*\mathrm{p} - \mathrm{X}^*||_2^2 + \alpha||\mathbf{L}\mathrm{p}||_2^2. \tag{S15}$$

Here, α is the regularization parameter and $\mathbf{L}$ is the second order finite difference operator, modified for fixed end points $p_0 = p_N = 0$ [17],

$$L = \frac{1}{2}\begin{pmatrix} 2 & 0 & & & & & & \\ -1 & 2 & -1 & & & & & \\ & -1 & 2 & -1 & & & & \\ & & . & . & . & & & \\ & & & -1 & 2 & -1 & & \\ & & & & -1 & 2 & -1 & \\ & & & & & 0 & 2 & \end{pmatrix} \tag{S16}$$

There are several variants of this specific regularizer $\mathbf{L}$ with different values for $L_{1,1} = L_{N,N}$ [18–20], but for the present problem, the choice of the boundary conditions has

marginal effect on the result. With this regularizer,

$$S = ||\mathbf{L}\mathrm{p}||_2^2 = \sum_{i=2}^{N-1} \left[p_i - (p_{i-1} + p_{i+1})/2\right]^2 + p_1^2 + p_N^2. \tag{S17}$$

The additional prefactor 1/2 to the first term in equation S15 ($\chi^2/2$) is introduced in anticipation of the Bayesian analysis further below. For practical reasons, the complex optical response function and the transfer matrix are separated into real and imaginary parts, combined with the regularization term,

$$\left|\left| \begin{pmatrix} \sigma^{-1}\mathbf{A}^{Re} \\ \sigma^{-1}\mathbf{A}^{Im} \\ \sqrt{2\alpha}\mathbf{L} \end{pmatrix} \mathrm{p} - \begin{pmatrix} \sigma^{-1}X^{Re} \\ \sigma^{-1}X^{Im} \\ 0_{N,1} \end{pmatrix} \right|\right|^2 \tag{S18}$$

and minimized using the MATLAB nonnegative linear least-square solver to provide p_α for the given value of α.

The regularization parameter was varied in a range covering three orders of magnitude with equal spacing on a logarithmic scale and the corresponding distribution functions p_α determined. There are several possible strategies for selecting the best choice for α [21,22]. We first applied the L-curve method [23,24] which is a graphical display of the balance between accurate data representation at small α and a smooth and regular solution at large α. For Tikhonov regularization, the L-curve is obtained by plotting the regularization penalty, $\hat{r} = \log||\mathbf{L}\mathrm{p}||_2$, vs. the model fit residual, $\hat{s} = \log||A^*\mathrm{p} - X^*||_2$, parameterized by the regularization parameter α, figure S10.

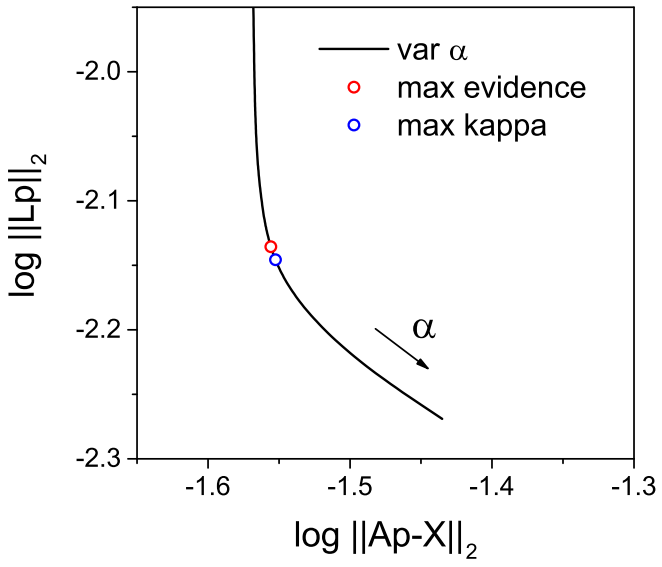

Figure S10: Close-up of the corner in the L-curve with point of maximum curvature and point of maximum evidence.

Suggested by Hansen *et al.*, the corner of the L-curve represents a well-balanced compromize and can be determined as the point of maximum curvature κ, [23]. Computation of the curvature using $\kappa = (\hat{r}'\hat{s}'' - \hat{r}''\hat{s}')/((\hat{r}')^2 + (\hat{s}')^2)^{3/2}$ involves the first and second derivatives of the discrete data $\hat{r}(\alpha)$ and $\hat{s}(\alpha)$, respectively, and requires preliminary smoothing (2nd order Sawitzky-Golay), figure S11. The resulting point of maximum curvature is marked in figure S10.

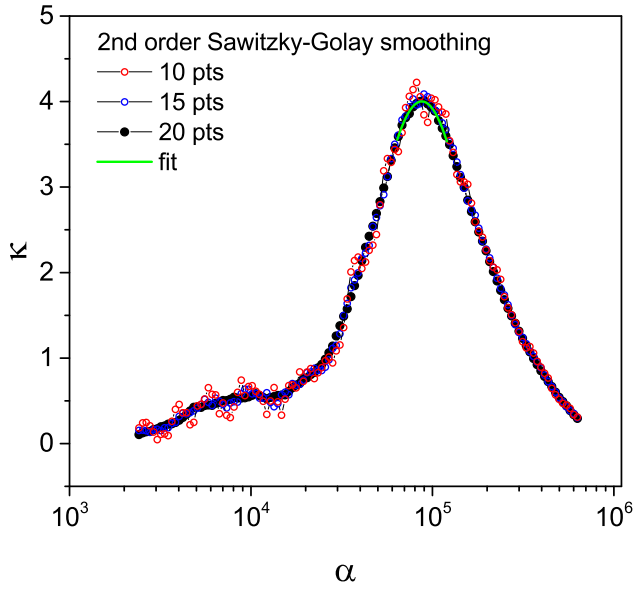

Figure S11: Curvature κ as function of regularization parameter α after 2nd order Sawatzky-Golay smoothing with different number of interpolation points. The maximum curvature was obtained by fitting a 2nd order polynomial.

An alternative approach for optimizing the regulatization parameter is provided by Bayesian probability theory. In the Bayesian framework, the Tikhonov regularization can be regarded as the first level of inference [25]. Given the hypothesis H that equation S14 is valid, the posterior propability of model parameter p after measurement X is the product of likelihood for the data and prior assumption for p, normalized by the evidence, i.e.

$$P(\mathrm{p}|X,H) = \frac{P(X|\mathrm{p},H)P(\mathrm{p}|H_i)}{P(X|H)} \tag{S19}$$

$$= \frac{exp(-\chi^2/2)exp(-\alpha S)}{P(X|H)}, \tag{S20}$$

The maximum *a posteriori* estimator (MAP) coincides with the minimum of the Tikhonov functional. Beyond this analogy, second level Bayesian inference also allows to evaluate the choice of α by comparing their evidence. The evidence, or marginal likelihood, serves as renormalization constant and is obtained by integrating the posterior probabilities. Taking advantage of the Laplace approximation for gaussian

posterior, as expected in the case of the Tikhononv regularization, the evidence for the regularization parameter α is [26]

$$P(\alpha) = C_N \exp\left(-\chi^2/2 - \alpha S\right) \cdot \det{}^{-1/2}(\mathbf{H}/\alpha). \tag{S21}$$

with $C_N = ((1/2)^N(N+1))^{1/2}$. The argument in the exponential is the Tikhonov functional evaluated at the MAP vector p_α. With the Hessian $\mathbf{H}$, computed as second derivative of $T(\mathrm{p})$ [20],

$$\begin{aligned}
\nabla_p T(\mathrm{p}) &= \nabla_p\big(\frac{1}{2\sigma^2}(\mathbf{A}\mathrm{p}-\mathrm{X})^T(\mathbf{A}\mathrm{p}-\mathrm{X}) + \alpha(\mathbf{L}\mathrm{p})^T(\mathbf{L}\mathrm{p})\big), && \text{(S22)}\\
&= \frac{1}{2\sigma^2}(2\mathbf{A}^T\mathbf{A}\mathrm{p} - 2\mathbf{A}\mathrm{X}) + \alpha(2\mathbf{L}^T\mathbf{L}\mathrm{p}), && \text{(S23)}\\
\mathbf{H} &\equiv \nabla_p^2 T(\mathrm{p}), && \text{(S24)}\\
&= \frac{1}{\sigma^2}\mathbf{A}^T\mathbf{A} + 2\alpha\mathbf{L}^T\mathbf{L}, && \text{(S25)}
\end{aligned}$$

the final posterior $\bar{\mathrm{p}}$ was obtained by summation of the subsolutions p_α, weighted by their evidence $P(\alpha)$, i.e.

$$\bar{\mathrm{p}} = \sum_{\alpha_{min}}^{\alpha_{max}} P(\alpha)\mathrm{p}_\alpha \Delta\alpha. \tag{S26}$$

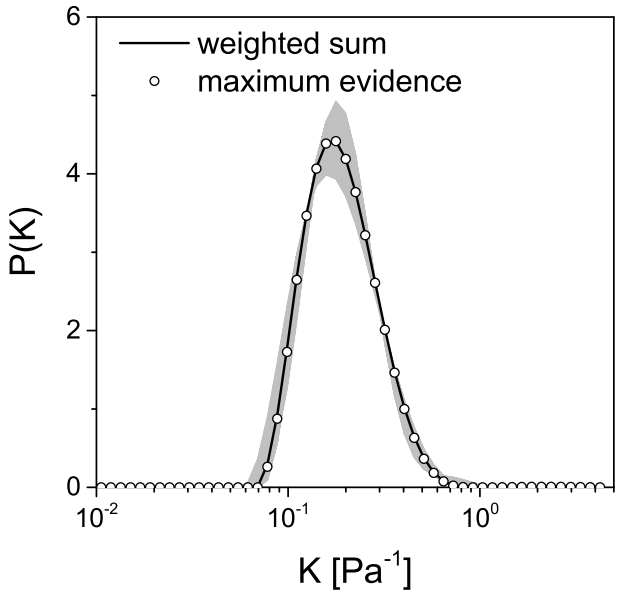

Figure S12: Density function P(K) obtained by Tikhonov regularization. The varying results for different α are represented by the gray area. Their sum, weighted by the evidence (equations S21 and S26) is well approximated by the particular density function for α with maximum evidence.

For the present inversion problem, the resulting weighted average solution $\bar{p}$ was found to be well approximated by the singular solution for maximum evidence α_{ME}. Furthermore, the value of α_{ME} was rather close to the point of maximum curvature in the L-curve, figure S10. The deviation in the distribution functions $P(K)$ was marginal as indicated by a difference in the expected mean E_K of less than 0.2%, figure S13. In conclusion, Tikhonov regulariation combined with parameter selection for maximum Bayesian evidence provides a convenient and reproducible method to retrieve the particle factor distribution function $P(K)$ from a calibration measurement.

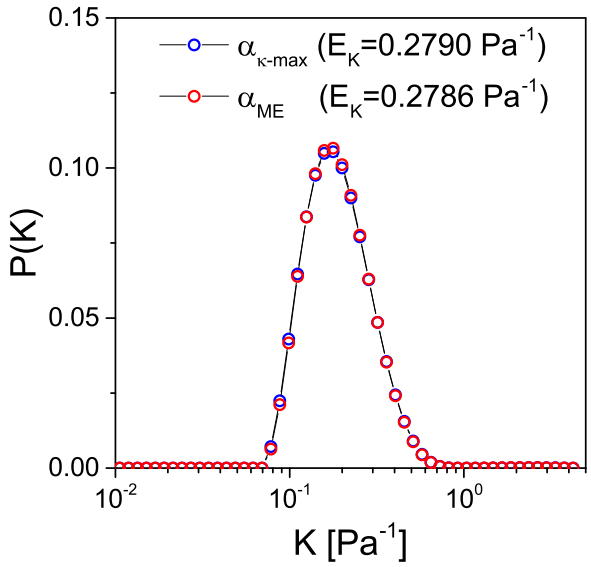

Figure S13: Comparison of the density function P(K) obtained by Tikhonov regularization for α at maximum curvature κ of the L-curve with the result for α with maximum evindence in the Bayesian inference.

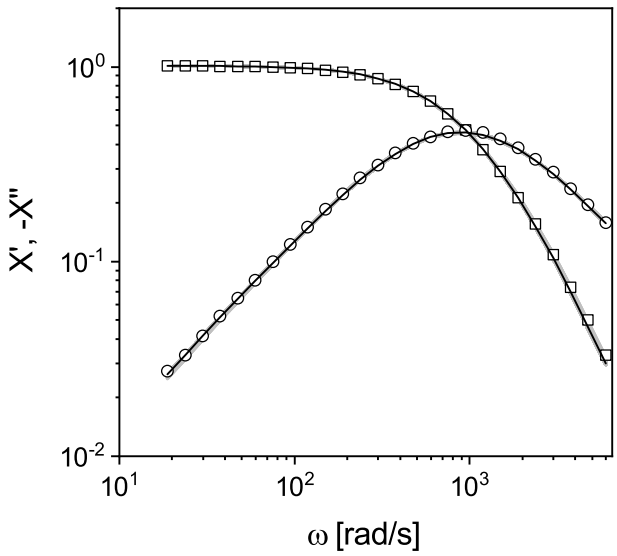

Figure S14: Fit of the real and imaginary part of the optical response function obtained by numerical inversion using Tikhonov regularization and optimized parameter α_{ME}.

S3.3 Linearity, resolution limit and viscosity range

We consider some experimental aspects of OFOT measurements which are relevant for the application in microrheology. The magnetic nanorods are actively driven to oscillatory rotation by the external field. Hence, the particle are not equilibrated with the polymer solution. In analogy to SAOS measurements, we check for the linear response regime by varying the oscillation angle amplitude β_0. As shown in Figure S15 using an example, the OFOT spectra are indentical within the experimental uncertainty when the oscillation amplitude is reduced from 12° to 1°. All OFOT measurements are routinely repeated using two angular amplitudes of (12° and 6°, respectively, and examples for all nanorods, used in the present study are shown in Figure S16.

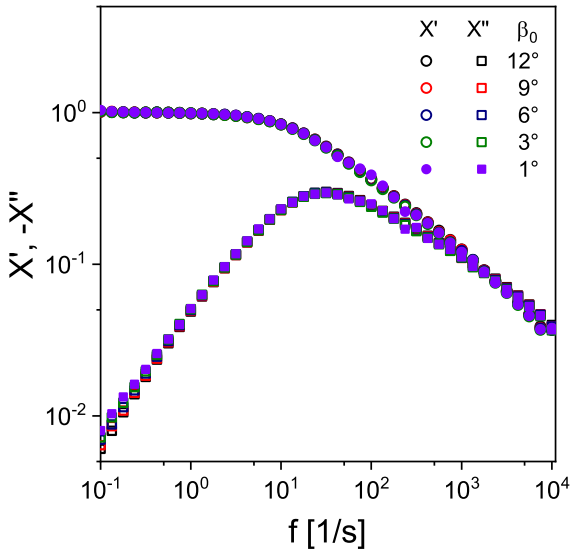

Figure S15: OFOT response functions of nanorods (L_h = 240 nm) in a 2.91 wt.% PEO-1M solution. Variation of the oscillation angle amplitude β_0 shows no significant effect on the result which confirms the measurements to be in the linear regime.

Another important figure is the lower resolution limit of the method. In Figure S17 we compare results obtained from different methods applied to 0.198 wt.% PEO-1M solution. The rolling ball viscometer provided $\eta_0 = 2.365(6)\,\mathrm{mPa \cdot s}$, i.e. slightly more than twice the viscosity of the solvent water. Shear rate-dependent viscosity measurements exhibit a slightly lower constant value at low shear rates and the onset of shear thinning a $\dot{\gamma} > 2000\,1/\mathrm{s}$. The dynamic modulus, obtained by SAOS or OFOT measurements can only be compared with shear rheometry on the basis of the Cox-Merz rule. The magnitude of the complex viscosity, derived from SAOS measurements, is in agreement with the shear viscosity. Shear thinning could not be revealed due to the limited frequency range. In contrast, the complex viscosity, calculated from OFOT spectra, clearly showed the decrease at high frequencies. However, we also observe some modulation in the data, which are presumably caused by small

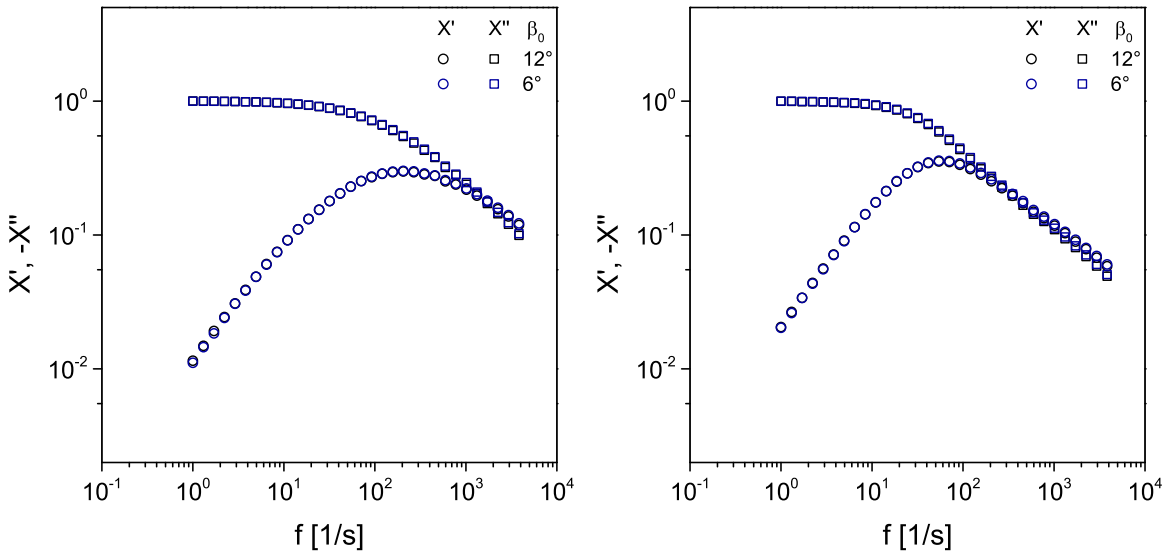

(a)

(b)

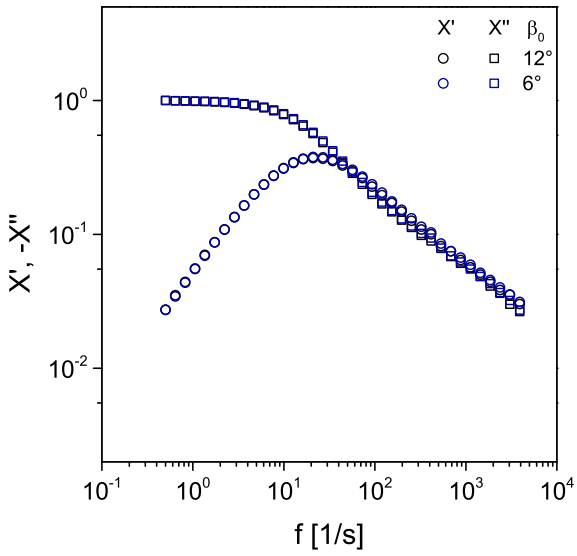

(c)

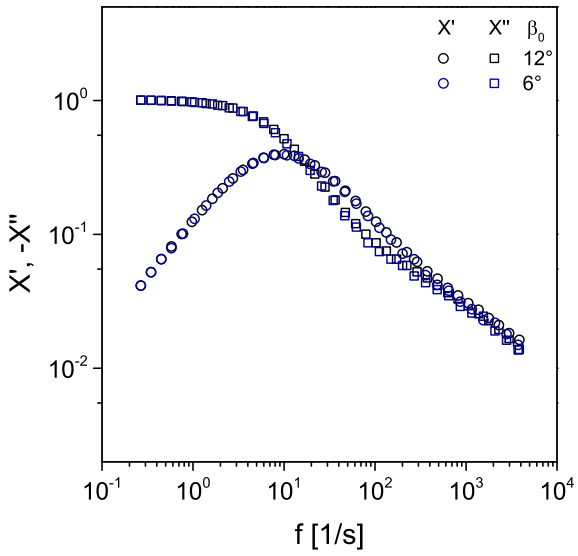

(d)

Figure S16: OFOT spectra of 2.91 wt.% PEO-1M solution measured with different nanorods (a) N2 (b) N3 (c) N4 (d) N5. All samples are measured at two oscillation angle amplitudes β_0 to verify the linear regime.

changes in the hydrodynamic profile $P(K)$ of the nanorod colloid. The standard deviation in the frequency range below 1000 rad/s is $\sigma_{eta_0} = 0.08\,\mathrm{mPa}\cdot\mathrm{s}$ and represents the resolution limit of the method at very low viscosities.

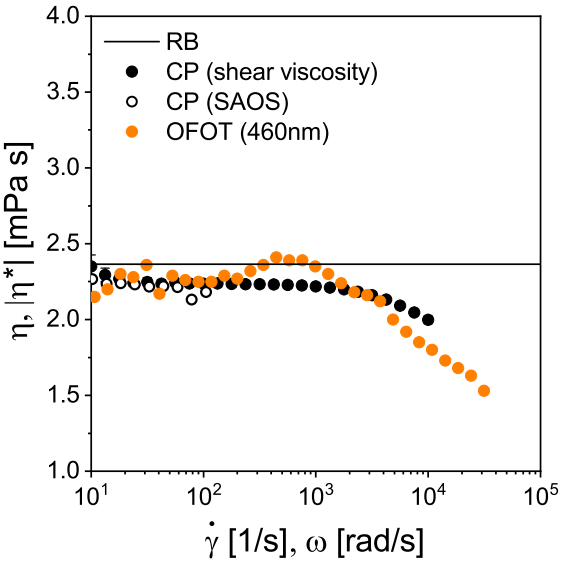

Figure S17: Shear Viscosity (CP) of 0.198 wt.% PEO-1M exhibits Newtonian regime at low shear rates, slightly lower than the result obtained from rolling ball viscosimetry, 2.365(6) mPas (horizontal line). The onset of shear thinning is observed at $\dot{\gamma} > 10^3\,1/\mathrm{s}$. The results are compared with the complex viscosity, derived from SAOS and OFOT measurements based on the Cox-Merz rule. The SAOS results agree with the zero shear rate viscosity but are restricted in the accessible frequency range. The viscosity derived from OFOT measurements agree in the low frequency range and also exhibit a decrease at $\omega > 10^3\,\mathrm{rad/s}$. The uncertainty, associated with the modulation of the signal, determines the resolution limit of the method.

The upper limit of OFOT measurement is apparent from the dynamic modulus measurements at high polymer concentrations, e.g. in Figure S23. For $|G^*| > 3\,\mathrm{kPa}$, the optical signal reaches the noise level of the present experimental setup so that the phase shift cannot be determined accurately.

S4 Additional evaluations according to alternative approaches

S4.1 Size-dependent viscosity according to Wisniewska *et al.*

Wisniewska *et al.* [27] analyzed a collection of literature data and provided a semi-empirical equation for the viscosity of PEO solutions,

$$\eta_0 = \eta_s \exp\left(\frac{\Delta E}{RT}\left(\frac{R_h}{R_g(c/c^*)^\beta}\right)^\alpha\right) \tag{S27}$$

with the model parameters $\Delta E = 4\,\mathrm{kJ/mol}$, $\alpha = 0.78$ and $\beta = 0.75$ for entangled solutions. Other quantities in eq S27 are the solvent viscosity η_s, gas constant R, temperature T, overlap concentration c^*, hydrodynamic radius R_h and radius of gyration R_g of the PEO molecules. For further details, we refer to the original publication [27]. When applied to the macroscopic zero-shear rate viscosity data, we find excellent agreement without further adjustment of the model parameters, figures S18 and S19 (black markers).

The model has been generalized to also describe the size-dependent viscosity, derived from the motion of small spherical particles with size R_p. Keeping all parameters fixed, only the hydrodynamic radius of the polymer R_h in the numerator is replaced by R_{eff} with $R_{eff}^{-2} = R_h^{-2} + R_p^{-2}$. The results for the viscosity, derived from OFOT measurements of the same solutions using Ni nanorods of different hydrodynamic length, are analyzed using Eq.S27 and the best approximate values for R_{eff} obtained by minimizing the mean square deviation are summarized in Table S3. The results are significantly smaller than the hydrodynamic length of the nanorods, however, they are rather close to values calculated using a modified relation $\tilde{R}_{eff}^{-2} = R_h^{-2} + (L_h D_h/4)^{-1}$, which takes the cylindrical shape with hydrodynamic length L_h and diameter D_h of the nanorods into account. Despite this apparently good agreement, the concentration dependence of the nanoviscosity is not reproduced very well. The measurements show a much stronger increase with c, comparable to the macroscopic viscosity, so that the ratio $\eta_0^{OFOT}/\eta_0^{macro}$ is nearly constant.

Table S3: Analysis of zero-shear rate viscosity obtained from OFOT measurements using eq S27: PEO molar mass M_w, hydrodynamic radius R_h, radius of gyration R_g and overlap concentration c^* (see reference [27]), hydrodynamic length of nanorods L_h (D_h = 50 nm for all nanorods), effective hydrodynamic size R_{eff}, obtained by minimization of mean square deviation, and $\tilde{R}_{eff}$, calculated using the hydrodynamic size of the nanorods.

M_w [g/mol]	R_h [nm]	R_g [nm]	c^* [g/cm^3]	L_h [nm]	R_{eff} [nm]	$\tilde{R}_{eff}$ [nm]
1M	39.1	68.5	0.0013	170	30.4	33.5
				298	33.3	35.5
				460	36.0	36.7
220k	16.3	28.0	0.0040	170	14.7	15.8
				298	15.5	16.0
				460	16.0	16.1

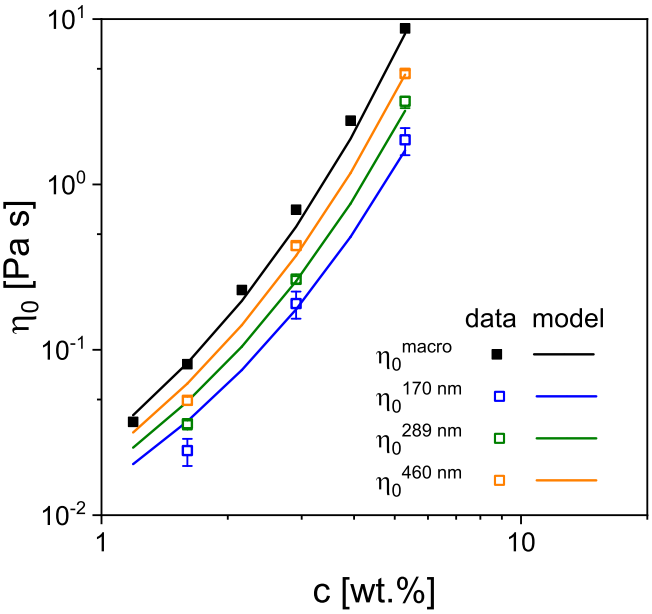

Figure S18: Zero-shear rate viscosity of PEO-1M solutions in the entanglement regime as function of concentration. The semi-empirical relationship (eq S27 shows excellent agreement with macroscopic viscosity (black markers) without adjusting parameters. The results obtained from OFOT measurements can be approximated by the size-dependent viscosity model by variation of R_{eff}, however, the predicted concentration dependence is weaker than observed in the experimental results.

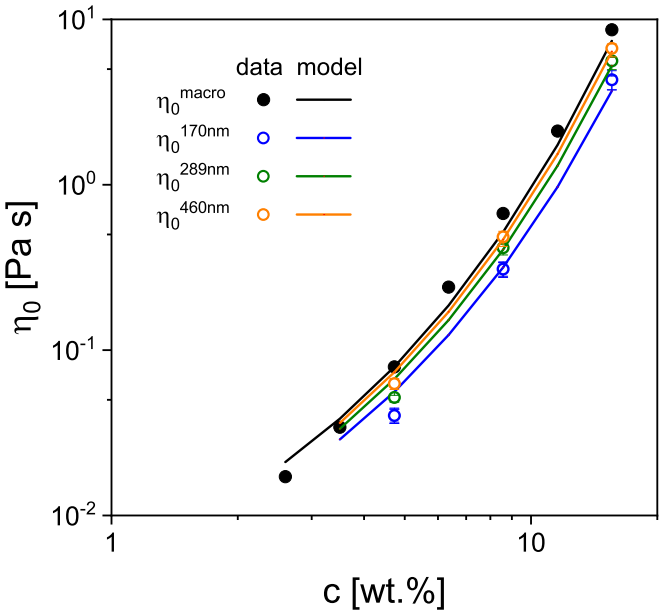

Figure S19: Zero-shear rate viscosity of PEO-220k solutions in the entanglement regime as function of concentration. The semi-empirical relationship (eq S27 shows excellent agreement with macroscopic viscosity (black markers) without adjusting parameters. The results obtained from OFOT measurements can be approximated by the size-dependent viscosity model by variation of R_{eff}, however, the predicted concentration dependence is weaker than observed in the experimental results.

S4.2 Correlation length as scaling parameter for the relative viscosity

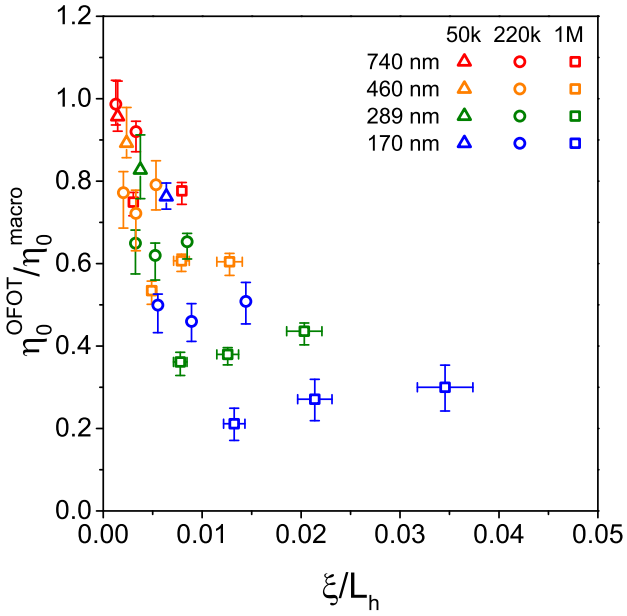

Figure S20: The ratio of zero-shear rate viscosities, retrieved from OFOT spectra, divided by the macroscopic values and plotted as function of ξ/L_h do not fall on a common master curve. For comparison, see Figure 8 in the main paper.

S4.3 Mathematical approximation of size scaling

The reduced zero-shear rate viscosities $\eta_0^{OFOT}/\eta_0^{macro}$ of PEO solutions with different molecular weight and concentration, and measured using nanorods with different hydrodynamic length, collapse on a master curve when plotted as function of R_g/L_h. A first attempt to identify an empirical relation is a log-log plot, shown in Figure S21. The data exhibit continuous curvature instead of a constant slope which rules out a simple power law dependence.

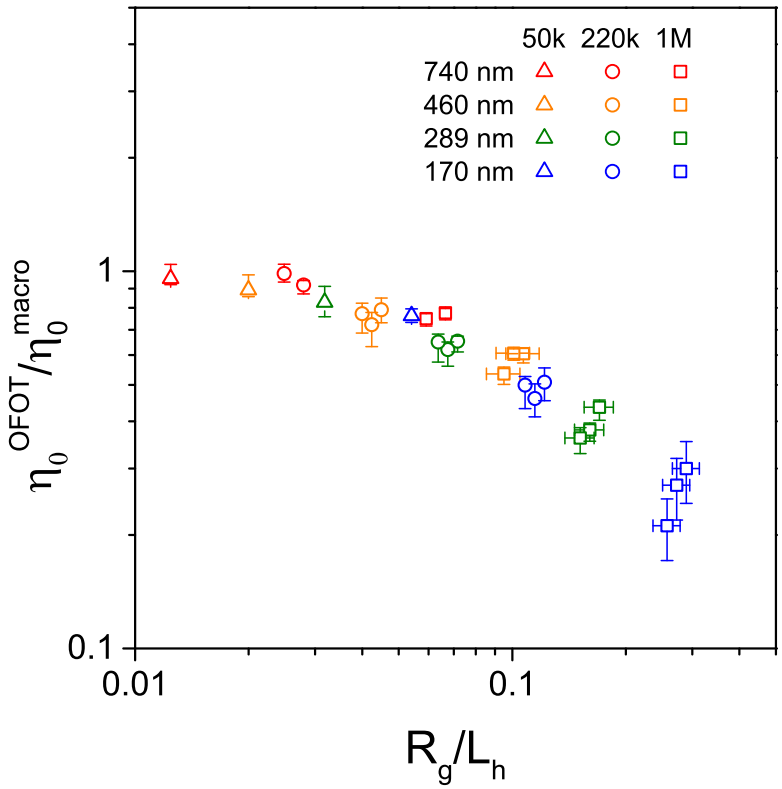

Figure S21: Log-log plot of reduced zero-shear rate viscosity as function of ratio R_g/L_h. The continuous curvature rules out a simple power law relation.

We further compare the least-square fit of the reduced zero-shear rate viscosity as function of R_g/L_h, shown in Figure S22, by (i) an exponential function and (ii) a linear relation. The residuum of the linear regression clearly exhibits a systematic deviation whereas that of the exponential fit a more homogeneous scatter.

S4.4 Constraint release by nanorod translational diffusion

Dispersed rigid particles contribute a geometric constraint to the lateral motion of macromolecules in addition to molecular entanglement. Consequently, stress release

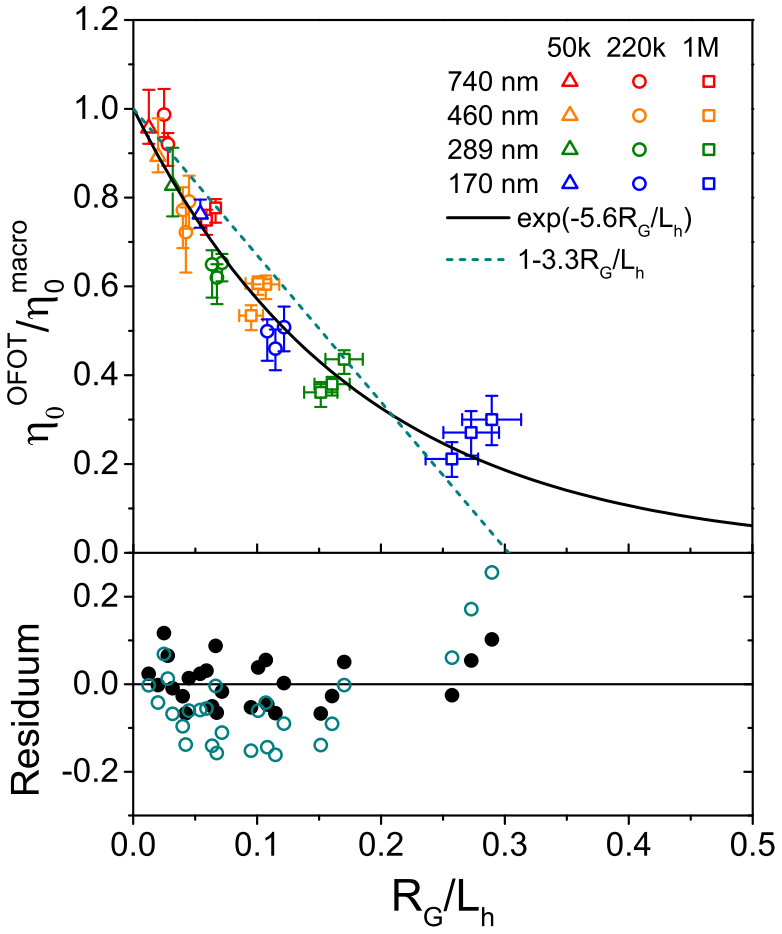

Figure S22: Comparison of linear and exponential fit of reduced zero-shear rate viscosity as function of ratio R_g/L_h. Upper pane Fit and lower pane, residuum.

may occur by particle diffusion addition to reptation and is dominated by the faster of the two processes. For comparison of the characteristic time constants, we first calculate the disengagement time $\tau_d = 3Z^3\tau_e$ from the analysis of SAOS data using the Likthman-McLeish model (Table). The particle escape time is calculated using $\tau_p = L_h^2/D$ with diffusion constant $D = k_BT\ln(L_h/D_h)/(n\pi L_h\eta_{eff})$ for translation parallel ($n = 2$) or perpendicular ($n = 4$) to the nanorod axis. Since the hydrodynamic diameter of the nanorods is close to the tube diameter, the particles are at the border between the large and intermediate size regime. With the low number of entanglements, the effective viscosity in the intermediate size regime, $\eta_{eff} \approx \eta_s(D_h/\xi)^2$, is similar to the macroscopic viscosity. Therefore, we estimate $\eta_{eff} \approx \eta_s(R_h/\xi)^2$ with the hydrodynamic radius $R_h = D_h/2$ as measure of particle size as a lower bound. The obtained particle escape times are all significantly larger than the reptation time, Table S4. Reptation, being the faster process in all solutions, determines the viscoelastic

behavior and constraint release by translational diffusion can be neglected.

Table S4: Analysis of characteristic times for stress relaxation by reptation or particle diffusion for PEO-1M solutions with concentration c: correlation length ξ, tube diameter a_t, effective viscosity in the intermediate regime η_{eff}, disengagement time by reptation τ_d and escape times of nanorods by diffusion parallel ($\tau_{p,||}$) or perpendicular ($\tau_{p,\perp}$) to the cylinder axis for particles with given hydrodynamic length.

c	[g/cm^3]	1.60	2.91	5.29
ξ	[nm]	5.9	3.4	2.0
a_t	[nm]	108	67	57
η_{eff}	[Pa · s]	0.067	0.201	0.581
τ_d	[s]	0.002	0.058	0.108
$\tau_{p,\|\|}$ (460 nm)	[s]	6.5	19.6	56.7
$\tau_{p,\|\|}$ (289 nm)	[s]	2.3	7.0	20.2
$\tau_{p,\|\|}$ (170 nm)	[s]	0.9	2.9	8.2
$\tau_{p,\perp}$ (460 nm)	[s]	0.3	1.1	3.3
$\tau_{p,\perp}$ (289 nm)	[s]	0.3	0.8	2.4
$\tau_{p,\perp}$ (170 nm)	[s]	0.3	1.0	2.8

S5 Dynamic modulus of PEO-220k solutions

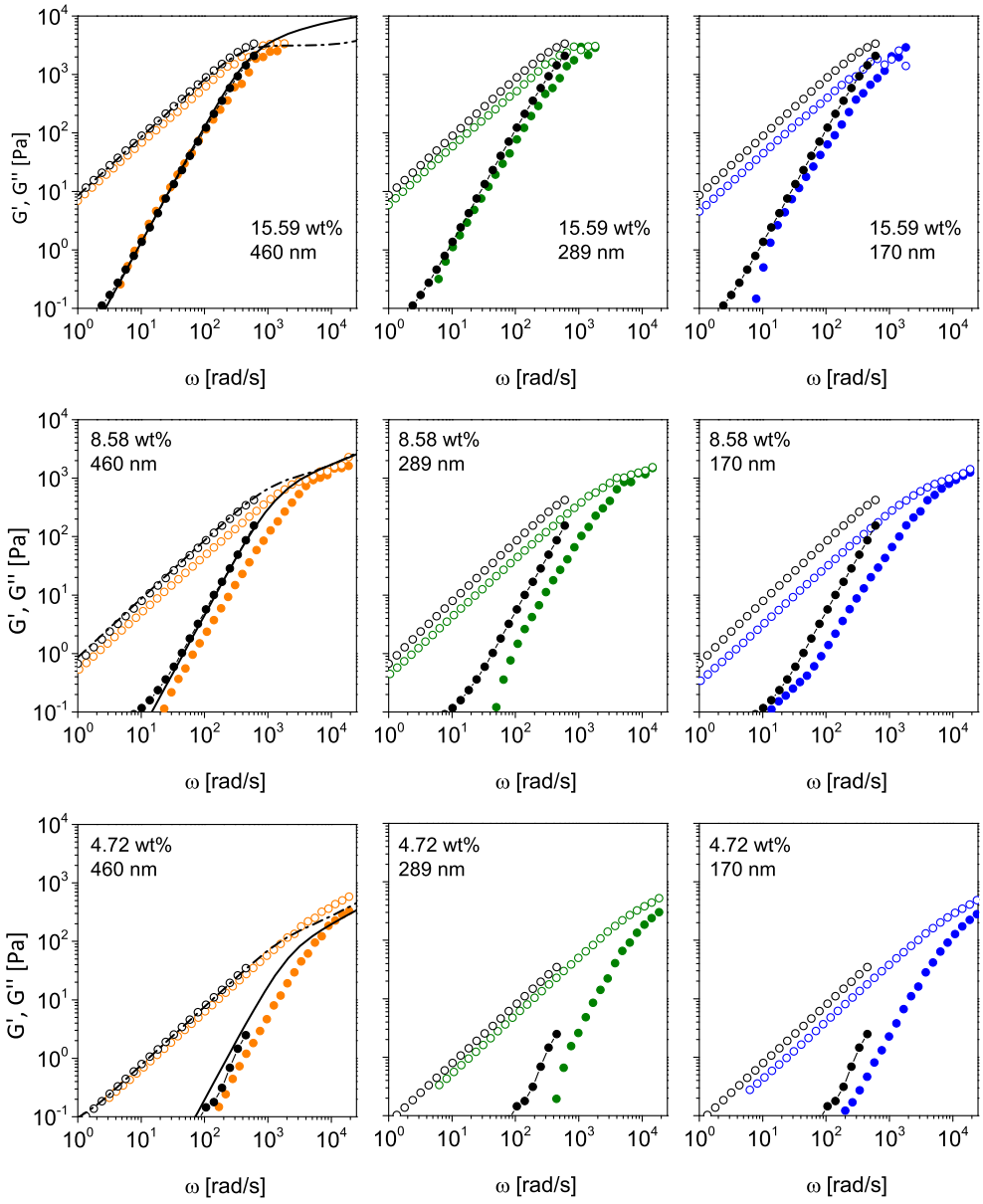

Figure S23: Dynamic modulus of PEO-220k solutions with three different concentrations (rows) determined from OFOT measurements using nanorods of different hydrodynamic size (columns). The macroscopic dynamic modulus (SAOS, black markers) is shown for comparison and the results from the Likhtman-McLeish model calculations (black lines) are also included in the left column.

Table S5: Parameters, used in Likhtman-McLeish model calculations: molar mass M_w and concentration c of the PEO-220k solutions, entanglement modulus G_e and molar mass M_e of an entanglement strand, number of entanglements per chain Z, and equilibration time constant τ_e.

M_w	c	G_e	M_e	Z	τ_e
[g/mol]	$[g/cm^3]$	[Pa]	[g/mol]	[1]	$\times 10^{-6}$ s
220k	15.59	17636	25400	8.7	3.8
220k	8.58	4185	59000	3.7	33
220k	4.72	992	136800	1.6	17

References

[1] Huggins, M. L. The viscosity of dilute solutions of long-chain molecules. iv. dependence on concentration. *J. Am. Chem. Soc.* **1942**, 64, 2716-2718.

[2] Kraemer, E. O. Molecular weights of celluloses and cellulose derivates. *Ind. Eng. Chem.* **1938**, 30, 1200-1203.

[3] Kawaguchi, S.; Imai, G.; Suzuki, J.; Miyahara, A.; Kitano, T.; Ito, K. Aqueous solution properties of oligo- and poly(ethylene oxide) by static light scattering and intrinsic viscosity. *Polymer* **1997**, 38, 2885-2891.

[4] Teraoka, I. Polymer Solutions: An Introduction to Physical Properties; John Wiley & Sons: New York, 2002.

[5] Rubinstein, M.; Colby, R. Polymer Physics; Oxford University Press: Oxford, 2003.

[6] de Gennes, P. G. Reptation of a polymer chain in the presence of fixed obstacles. *J. Chem. Phys.* **1971**, 55, 572-579.

[7] Doi, M.; Edwards, S. F. The Theory of Polymer Dynamics; Clarendon Press: Oxford, 1988.

[8] Likhtman, A. E.; McLeish, T. C. B. Quantitative theory for linear dynamics of linear entangled polymers. *Macromolecules* **2002**, 35, 6332-6343.

[9] Doi, M. Explanation for the 3.4-power law for viscosity of polymeric liquids on the basis of the tube model. *J. Polym. Sci.: Polym. Phys. Ed.* **1983**, 21, 667-684.

[10] Rubinstein, M.; Colby, R. H. Self-consistent theory of polydisperse entangled polymers: Linear viscoelasticity of binary blends. *J. Chem. Phys.* **1988**, 89, 5291-5306.

[11] Ramirez, J.; Boudara, V. Reptate (rheology of entangled polymers: Toolkit for analysis of theory & experiment). free and open-source software package, https://reptate.readthedocs.io/, 2018.

[12] Larson, R. G.; Sridhar, T.; Leal, L.G.; McKinley, G. H.; Likhtman, A. E.; McLeish, T. C. B. Definitions of entanglement spacing and time constants in the tube model. *J. Rheol.* **2003**, 47, 809-818.

[13] de Gennes, P. G. Scaling Concepts in Polymer Physics; Cornell University Press: Ithaca, New York, 1979.

[14] Krämer, F.; Gratz, M.; Tschöpe, A. Analysis of the static magnetic field-dependent optical transmission of Ni nanorod colloidal suspensions. *J. Appl. Phys.* **2016**, 120, 044301.

[15] Tschoegl, N. W. The Phenomenological Theory of Linear Viscoelastic Behavior; Springer: Berlin Heidelberg, 1989.

[16] Diaz-Calleja, R.; Garcia-Bernabé, A.; Sanchis, M. J.; del Castillo, L. F. Interconversion of mechanical and dielectrical relaxation measurements for dicyclohexylmethyl-2-methyl succinate. *Phys. Rev. E* **2005**, 72, 051505.

[17] Bender, P.; Balceris, C.; Ludwig, F.; Posth, O.; Bogart, L. K.; Szczerba, W.; Castro, A.; Nilsson, L.; Costo, R.; Gaviln, H.; Gonzlez-Alonso, D.; de Pedro, I.; Fernandez Barqun, L.; Johansson, C. Distribution functions of magnetic nanoparticles determined by a numerical inversion method. *New J. Phys.* **2017**, 19, 073012.

[18] Vestergaard, B.; Hansen, S. Application of bayesian analysis to indirect fourier transformation in small-angle scattering. *J. Appl. Crystallogr.* **2006**, 39, 797-804.

[19] Hansen, S. Estimation of the relaxation spectrum from dynamic experiments using bayesian analysis and a new regularization constraint. *Rheol. Acta* **2008**, 47, 169-178.

[20] Bui-Thanh, T. A gentle tutorial on statistical inversion using the bayesian paradigm. *ICES Report* **2012** 12-18.

[21] Gábor, A.; Banga, J. R. Robust and efficient parameter estimation in dynamic models of biological systems. *BMC Syst. Biol.* **2015**, 9, 74.

[22] Zou, Y.-L.; Xie, R.-H.; Arad, A. Numerical estimation of choice of the regularization parameter for NMR t2 inversion. *Pet. Sci.* **2016**, 13, 237-246.

[23] Hansen, P. C.; O'Leary, D. P. The use of the l-curve in the regularization of discrete ill-posed problems. *SIAM J. Sci. Comput.* **1993**, 14, 1487-1503.

[24] Hansen, P. C. The l-curve and its use in the numerical treatment of inverse problems. In Computational Inverse Problems in Electrocardiology; Johnston, P. ed.; WIT Press: Southampton, 2000; Vol. 5, p. 119. .

[25] MacKay, D. J. C. Bayesian interpolation. *Neural Comput.* **1992**, 4, 415-447.

[26] Hansen, S. Bayesian estimation of hyperparameters for indirect fourier transformation in small-angle scattering. *J. Appl. Crystallogr.* **2000**, 33, 1415-1421.

[27] Wisniewska, A.; Sozanski, K.; Kalwarczyk, T.; Kedra-Krolik, K.; Pieper, C.; Wieczorek, S. A.; Jakiela, S.; Enderlein, J.; Holyst, R. Scaling of activation energy for macroscopic flow in poly(ethylene glycol) solutions: Entangled non-entangled crossover. *Polymer* **2014**, 55, 4651-4657.